

Article

Accurate Fruit Phenotype Reconstruction via Geometry-Smooth Neural Implicit Surface

Wei Ying ^{1,†} , Kewei Hu ² , Ayham Ahmed ² , Zhenfeng Yi ¹, Junhong Zhao ^{3,†} and Hanwen Kang ^{2,*} 

¹ College of Engineering, South China Agriculture University, Guangzhou 510642, China; yingwei@stu.scau.edu.cn (W.Y.); yizhenfeng_wind@163.com (Z.Y.)

² Department of Mechanical and Aerospace Engineering, Monash University, Clayton, VIC 3800, Australia; kewei.hu1@outlook.com (K.H.); ayham.ahmed@monash.edu (A.A.)

³ Institute of Facility Agriculture, Guangdong Academic of Agriculture Science, Guangzhou, 510640, China; zhaojunhong@gdaas.cn

* Correspondence: hanwen.kang1@monash.edu

† These authors contributed equally to this work.

Abstract: Accurate collection of plant phenotyping is critical to optimising sustainable farming practices in precision agriculture. Traditional phenotyping in controlled laboratory environments, while valuable, falls short in understanding plant growth under real-world conditions. Emerging sensor and digital technologies offer a promising approach for direct phenotyping of plants in farm environments. This study investigates a learning-based phenotyping method using neural implicit surfaces reconstruction to achieve accurate *in situ* phenotyping of pepper plants in greenhouse environments. To quantitatively evaluate the performance of this method, traditional point cloud registration on 3D scanning data is implemented for comparison. Experimental result shows that NIR (neural implicit surfaces reconstruction) achieves competitive accuracy compared to the 3D scanning method. The mean distance error between the scanner-based method and the NeRF (neural radiance fields)-based method is 0.811 mm. This study shows that the learning-based NeRF method has similar accuracy to the 3D scanning-based method but with greater scalability and faster deployment capabilities.



Citation: Ying, W.; Hu, K.; Ahmed, A.; Yi, Z.; Zhao, J.; Kang, H. Accurate Fruit Phenotype Reconstruction via Geometry-Smooth Neural Implicit Surface. *Agriculture* **2024**, *14*, 2325. <https://doi.org/10.3390/agriculture14122325>

Academic Editor: Margarita García-Vila

Received: 15 November 2024

Revised: 15 December 2024

Accepted: 16 December 2024

Published: 19 December 2024



Copyright: © 2024 by the authors. Licensee MDPI, Basel, Switzerland. This article is an open access article distributed under the terms and conditions of the Creative Commons Attribution (CC BY) license (<https://creativecommons.org/licenses/by/4.0/>).

1. Introduction

Artificial intelligence has facilitated the rapid development of precision agriculture, which is significantly more efficient and productive than traditional production methods [1]. In precision agriculture, the measurement of plant phenotypes is of critical importance. Phenotyping provides a rapid understanding of the traits expressed by genes with complex structures and helps to understand genetic characteristics for different plant functions [2,3]. Phenotyping is a complex and challenging task due to the numerous characteristics of genotypes [4,5]. Plant breeders use manual measurement of phenotypic data, which is an expensive, labour-intensive and time-consuming process. Therefore, there is a current need for easier and more accurate phenotyping measurements [6].

Two-dimensional imaging can be achieved with an RGB camera to measure basic morphological features of the plant such as colour, shape and texture. However, the geometric appearance is missing because the data are limited to two dimensions [7]. Three-dimensional imaging systems can capture basic geometric features of plants, such as volume, stem angle and projected canopy area, with high quality. In addition, 3D methods can track plant growth and yield over time, helping researchers to make phenotyping judgments [8,9]. High-quality 3D reconstruction models can be used to characterise leaves, estimate crop yields and classify fruits [10,11]. In recent years, several technological

approaches have been developed to quickly and accurately acquire three-dimensional data on plant morphology and structure.

NeRF, a neural radiance fields approach for Novel View Synthesis, enables the rapid reconstruction of 3D models by learning information from 2D images [12]. In various scenarios, NeRF can offer valuable insights that are hard to obtain using 2D data alone. This is achieved by incorporating multiview data, which helps to overcome the limitations caused by occlusions and crossings in plant structures. NeRF can reconstruct the distance, orientation and light of the plant, providing new perspectives. Despite being an implicit field representation, NeRF stores density information in the neural network, which serves as a crucial database for later geometric extraction.

Although there have been advancements, challenges still exist with the current method of acquiring phenotyping data. Firstly, conventional scanners are very expensive and require specific acquisition environments, while the post-processing of point cloud data is complicated, which leads to longer modelling times. In addition, 3D reconstruction methods based on MVS require high-resolution and precise measurements, as well as continuous acquisition of multiview images. Although current 3D phenotypic reconstruction methods of neural radiation fields produce high-quality geometries, the lack of actual dimensions of the scene affects the data measurements. Furthermore, the lack of optimisation in plant scenes results in poor reconstruction quality.

This study aims to develop a highly accurate fruit phenotypic reconstruction method using the principle of neural radiance fields (NeRF). Compared to previous work developing the NeRF framework for plant phenotyping [13], this research focuses on generating high-quality fruit geometry models with fine details. This approach enables precise phenotypic measurement of fruits using only multiview synthesis, eliminating the need for expensive 3D scanning devices and their cumbersome data acquisition process. Specifically, the contributions of this study are as follows:

- Introduce a novel implicit surface network, Geometry-Smooth Neural Implicit suRface (GS-NIR), focusing on improving the quality of geometry reconstruction, showing an enhanced performance in fruit phenotyping.
- Deploy a sparse neural network for instance segmentation on reconstruction results and process phenotypic data.
- Implement a robotic data acquisition and phenotyping process based on the above two innovations, as shown in Figure 1.



Figure 1. Phenotyping robot operating in greenhouse and its reconstructed local geometry model.

The rest of this paper is organised as follows. Section 2 surveys related work. Section 3 details the GS-NIR model and methods for automated phenotypic data processing and measurement. Section 4 is a discussion of the results and details of the experiments. The conclusion is in Section 5.

2. Related Works

2.1. Recent Plant Phenotyping

Phenomics is an emerging field of research that quantifies animal and plant traits in multiple dimensions [11]. It provides comprehensive scientific knowledge that is no longer limited to the study of a single trait [14]. Typically, traditional phenotypic collections require dedicated measurement equipment such as structured light cameras [15], Time of Flight (ToF) cameras [16] and LiDAR [17] to measure various traits such as plant colour, shape and spatial structure. Structured light cameras project a fixed pattern of light onto the scene, compare the original pattern with the received distorted pattern and calculate the depth [18]. However, structured light cameras are less robust under complex lighting conditions and require very precise correspondence between images. ToF cameras use light emitted from an LED light source to build a 3D image by measuring the round-trip time between the emission of a light pulse and the reflection of a point [19]. LiDAR emits a laser that sweeps across the scene, and by calculating the laser return time, a 3D point cloud of the scene is obtained [20,21]. LiDAR provides more accurate 3D geometric information and can adapt to complex lighting conditions [22–24]. However, laser scanners can be slow and at high frequencies may heat or even damage plants. All of the above are expensive to acquire and maintain and also require complex processing steps and transmitting and receiving sensors [9]. Therefore, most of them can only be collected in the laboratory as they are susceptible to environmental factors [25,26].

Explicit modelling reconstruction is an important method for phenotype reconstruction. The reconstruction of a 3D point cloud can be achieved through the collection of 2D colour image data obtained from a camera. The most common applications include Multi-View Stereo (MVS) and Structure from Motion (SfM) [27]. SfM involves taking multiple photos from different unknown angles and matching the image features to estimate the camera position and depth information. MVS uses multiple cameras to generate parallax from different viewpoints and calculates the viewpoint object distance difference (triangulation) to obtain point cloud information [28]. Jay et al. [29] used a digital camera to capture continuous images and incorporated an SfM approach to reconstruct field crop models. Zermas et al. [30] extracted the geometry of maize stalks and leaves and extracted phenotypic features through a combination of drone and camera and 3D reconstruction using SfM. Furthermore, 3D reconstruction of apples and oranges was performed by a stereo vision system [31,32]. The accuracy of the above methods to estimate depth depends on the quality of feature matching [33]. In addition, lighting variations, image quality, repetitive texture structures or scene discontinuities can affect the accuracy of depth estimation and are prone to outliers and noise.

2.2. Neural Implicit Approaches

The technique of encoding spatial scenes in a neural network by learning continuous mathematical functions is called Neural Implicit Reconstruction. It is particularly adept at describing complex topologies and continuous surfaces. NeRF-based approaches [12] achieve accurate scene density values through basic ray tracing and volume rendering. 3DGS is a method based on a learning-based Gaussian kernel that yields high-quality renderings but poor-quality surface reconstruction [34]. The training speed of a model is constrained by the complexity of the neural network, and Instant-NGP introduced multiresolution hash tables and voxel representations to significantly improve reconstruction speed [35]. While the density field reconstruction method can achieve high rendering quality, it may lack high-precision surface information. NeuS [36] and VolSDF [37] proposed the Signed Distance Function (SDF) to improve the quality of surface reconstruction by imposing model constraints. Instant-NSR [38] and NeuS2 [39] improved the reconstruction speed without degrading the reconstruction quality by combining the advantages of hash coding and SDF. The efficient computation of a numerical gradient for hash grids proposed by Neuralangelo [40] solves the problem of non-smoothness of the learned surface in the hybrid method. However, the large weights used for model training often require image

compression during the training phase. Consequently, this compression can lead to the loss of the true size of the model after reconstruction, making phenotypic measurements impossible. In particular, most of the NeRF models are optimised only on standard datasets and lack an optimised approach for all types of plant scenarios, which can encounter uncontrollable factors in plant scenarios that can affect the quality of the reconstruction.

This research proposes geometric constraints and sampling strategies to address the problem of poor reconstruction quality present in plant scenes. Furthermore, an automated phenotype processing platform was developed by combining sparse neural networks and scale recovery algorithms, which effectively eliminates the scale error present in NeRF and enhances the robustness of agricultural scenarios.

3. Materials and Methods

This method has three components: (1) GS-NIR, based on the NeRF model, in which two improvements are proposed for the plant scene, introducing geometric depth smoothing constraints and a sampling strategy optimisation as shown in Figure 2; (2) a phenotype extraction network based on sparse neural networks; and (3) an automated phenotype extraction platform developed based on the above two components.

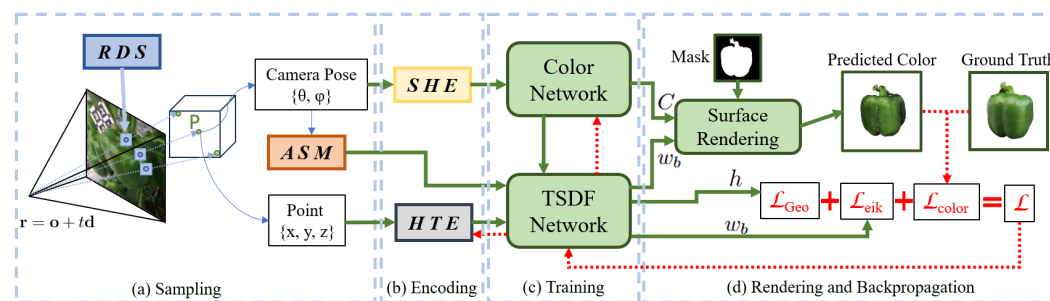


Figure 2. Pipeline of GS-NIR model. (a) is the sampling module, which generates the camera poses and coordinates according to the random dilation sampling (RDS) strategy and calculates the scene size by the adaptive scene module (ASM). (b) is coding module, which encodes the poses with Spherical Harmonics Encoding (SHE), and the point coordinates with Hash Table Encoding (HTE). (c) is the network training. (d) is the surface rendering and reconstruction, finally, according to the loss function and the backpropagation.

3.1. Neural Surfaces Revisited

The Neural Implicit Surfaces Model utilises SDF instead of density to represent the scene [38], still using position coordinates (x, y, z) and camera pose (θ, ϕ) as the basic input to the model. By randomly selecting pixel points of the image, emitting rays $\mathbf{r} = \mathbf{o} + t \mathbf{d}$ and sampling, the MLP predicts the SDF weights and colour values, and finally, the pixel colour is obtained according to the rendering formula, the rendering equation is

$$C(\mathbf{o}, \mathbf{v}) = \int_0^{+\infty} w_b(t) c(\mathbf{p}(t), \mathbf{v}) dt, \quad (1)$$

where $\mathbf{p}(t)$ is the point on a ray from a pixel, \mathbf{v} is the ray direction and $w_b(t)$ is the unbiased weight denoting the SDF; the set of equations is

$$\phi_b(f(x)) = \frac{be^{-b\pi(f(x))}}{(1 + e^{-b\pi(f(x))})^2}, \pi(f(x)) = \frac{1 - e^{-b f(x)}}{1 + e^{-b f(x)}}, \quad (2)$$

$$w_b(t) = \frac{\phi_b(f(\mathbf{p}(t)))}{\int_0^{+\infty} \phi_b(f(\mathbf{p}(u))) du}, \quad (3)$$

where $f(x)$ is the SDF value ($\mathbf{S} = \{x \in \mathbb{R}^3 | f(x) = 0\}$) predicted by the MLP, function $\phi_b(\cdot)$ is the logistic density distribution and the sigmoid function $\pi(\cdot)$ can truncate the SDF value range of -1 to 1 .

The NeRF model relies only on the pixel colours of each image to supervise the representation of the scene. This can be simple and fast to obtain a continuous scene, but there are some problems. When the image encounters high-reflectance plants during acquisition and the lighting conditions cannot be controlled, the high-reflectance areas will only retain white pixels on the image, and this discontinuous colour mutation will make the model inaccurate in predicting the depth values and at the same time affect the prediction of the SDF values, which ultimately leads to poor reconstruction quality.

In addition, the original NeRF-based reconstruction models all use the strategy of randomly selecting sampling points. Random points are not conducive to the prediction of depth values in continuous areas and are more likely to produce depth prediction errors. Meanwhile, it is difficult to maintain the optimal sampling viewpoint and sampling distance in complex agricultural scenes, which affects the construction of the whole scene.

3.2. GS-NIR Architecture

3.2.1. Geometric Depth Smoothing Constraints

To obtain more accurate depth values and predict more precise SDF values, geometric depth smoothing constraints have been proposed to limit the occurrence of drastic changes in local depth values, as shown in Figure 3. Specifically, the constraint method is as follows:

$$\begin{aligned}\mathcal{L}_{Geo} &= \sum_i \sum_{j \in \mathcal{N}(i)} \tau(i, j) \|h(i) - h(j)\|_1, \\ \tau(i, j) &= \exp(-\mu \|\mathbf{C}(i) - \mathbf{C}(j)\|_1)\end{aligned}\quad (4)$$

where h is the depth value, which can be estimated by calculating the termination depth when $f(x) = 0$, i is the pixel starting point corresponding to the sampling ray, $\mathcal{N}(i)$ is the nearby region to be smoothed, \mathbf{C} is the corresponding pixel colour value on the image and μ is the hyperparameter. $\tau(i, j)$ is a factor that reweights the colour gradient, as depth continuity tends to keep the colour continuous. This ensures that there is no excessive smoothing and protects the edges of the object. Local depth smoothing is more commonly used in traditional multiview reconstruction, and in order to apply this constraint in the training of the neural implicit field, calculations were performed using pixels as units instead of blocks.

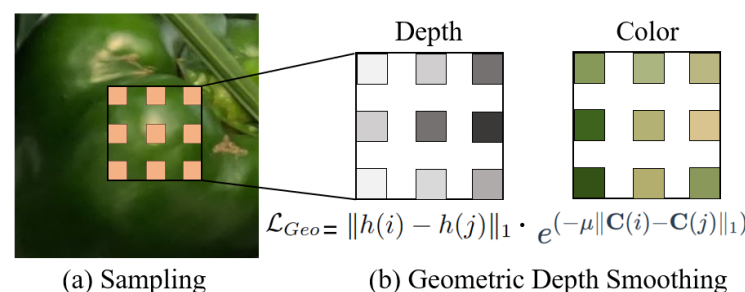


Figure 3. Illustration of proposed Geometric Depth Smoothing Constraints. **(a)** is the sampling point. **(b)** is the process of obtaining the depth and colour values from the sampling points and performing Geometric Depth Smoothing Constraints.

3.2.2. Sampling Strategy Optimisation

Two methods are adopted to perform sampling during training.

a. Random dilation sampling (RDS): In most NeRF models, the method used is often to randomly select a batch of pixel points in an image for ray tracing and set the sampling points. This strategy can greatly improve the efficiency of training and save GPU capacity. After a certain amount of training, good renderings can still be obtained. However, with

full random sampling, there is no way to ensure the continuity of the depth values, and an exact depth smoothing constraint is not possible.

To address this issue, the random expansion sampling strategy is proposed, as shown in Figure 4. First, a random batch of centre points are selected, and then 3×3 pixel points, called sampling kernels, are selected in the region adjacent to the centre points. This avoids the discontinuity of the fully random sampling points and ensures that the depth smoothing is effective in the region. Second, in order to expand the sampling range, the sampling kernel is expanded so that each pixel is separated by a certain distance. Dilated Convolution has been widely used in classical convolutional neural networks, which increases the collection of information without changing the feature map size. In neural implicit surfaces, the optimised strategy not only expands the sampling area but also improves the training efficiency.

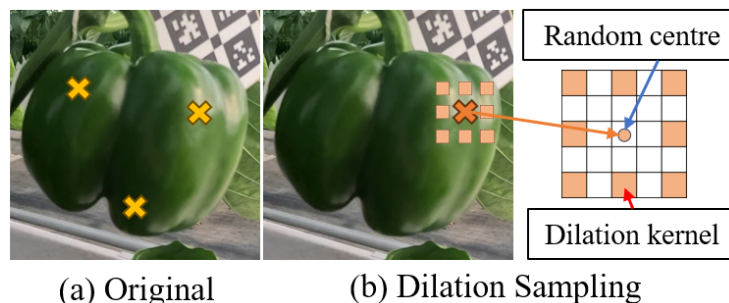


Figure 4. Illustration of proposed random dilation sampling. (a) is the sampling method in the original method. (b) is a demonstration of the random dilation sampling we used.

b. Adaptive scene module (ASM): As agricultural scenarios present disturbing factors such as complex landscapes and leafy branches, it is not possible to guarantee that the target is always in the centre during image acquisition, which can lead to reconstructed targets that are not in the centre or are only partially in the scene when building the 3D scene. To solve the above problems, the adaptive scene module is proposed. First, a system of linear equations is created for the camera origin position \mathbf{p}^* and line-of-sight direction \mathbf{d} :

$$\begin{bmatrix} \mathbf{d}_k^T \\ -\mathbf{d}_{k-1}^T \end{bmatrix} x = \mathbf{p}^{*k-1} - \mathbf{p}^{*k}. \quad (5)$$

Then the scene centre equation obtains the mean centre of all cameras. The equations is

$$\text{Centre} = \frac{1}{N} \sum_{k=1}^N (\mathbf{p}^{*k} + \mathbf{d}_k \cdot x_k). \quad (6)$$

After obtaining the scene centre, the scene size can be estimated by calculating the average distance between the camera centre and the scene centre. With the scene size, the reconstruction radius can be controlled to obtain the best reconstruction quality. Following many experiments, good reconstruction results were obtained by setting the radius (hyperparameter) to 0.75.

3.2.3. Network Training

In the GS-NIR model, the neural network consists of two components: Color Network and TSDF Network. The use of HTE (Hash Table Encoding) to encode the position coordinates and SHE (Spherical Harmonics Encoding) to encode the camera poses [35] can increase the dimensionality of the features, allowing the MLP to learn better. The input to the colour network consists of the SHE-encoded values and the hidden vectors output from the SDF network. The backbone network uses an MLP structure containing 2 hidden layers, each holding 64 neurons. The final output is the predicted colour values. The TSDF network takes as input the values of the position coordinates after HTE. The backbone

network uses an MLP structure containing 1 hidden layer holding 64 neurons. The network predicts the SDF values and hidden vectors to pass to the colour network. The overall loss used to optimise GS-NIR is a weighted combination of colour loss \mathcal{L}_{color} , gradient clamping \mathcal{L}_{eik} and geometric constraints \mathcal{L}_{Geo} :

$$\mathcal{L}_{color} = \sum_{r \in R} ||C_{pred}(r) - C_{gt}(r)||_2^2, \quad (7)$$

$$\mathcal{L}_{eik} = \sum_{j \in R} (\|\nabla f(\mathbf{x}_j)\|_2 - 1)^2, \quad (8)$$

$$\mathcal{L}_{total} = \alpha \mathcal{L}_{color} + \beta \mathcal{L}_{eik} + \gamma \mathcal{L}_{Geo} \quad (9)$$

After obtaining the \mathcal{L}_{total} , the parameters of network weights and HTE are optimised by backpropagation, and the direction of propagation is shown as the red line in Figure 2.

In addition, a mask, which defines the reconstructed target and background, is added to the training and used to eliminate disturbances in the scene, such as leaves or neighbouring fruits. Eliminating the background further improves the mesh resolution of the reconstructed target, which saves computational cost and reduces the reconstruction time.

3.3. Sparse Neural Network on Geometry Processing

Pepper segmentation and measurement is another core task of this study [41,42]. This method uses the sparse neural network architecture, Fuse-Pointnet++ [24], which is a previous work proposing an improved point mesh structure for semantic segmentation of fused 3D point clouds. The network has two components, including a backbone network for point cloud segmentation and components for space subdivision and concatenation, respectively. Fuse-Pointnet++ is the backbone of the network as it can accurately segment the point cloud after multimodal fusion. The colour values are entered into a single SA block used to collect the colour features, and the colour features are fused after processing the point features. The spatial subdivision component uses an octree to divide the scene into blocks and limit the points within the blocks as appropriate. Spatial subdivision solves the problem that the backbone network is unable to input a large number of point clouds at a single time, and after subdivision, the network can handle more than 100k points at one time. The network architecture of the Fuse-PointNet++ model is shown in Figure 5.

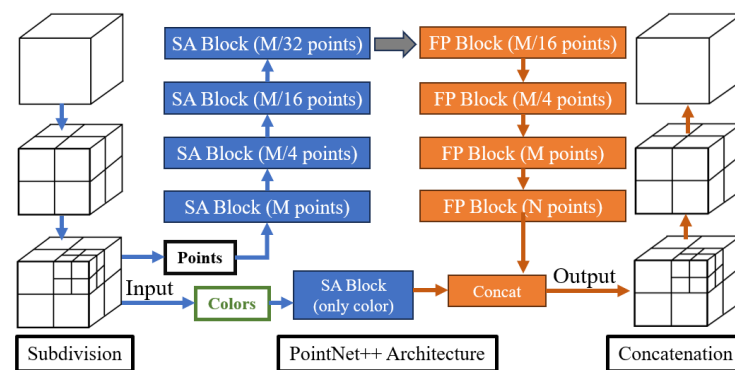


Figure 5. Illustration of proposed 3D semantic segmentation method. Input data are point cloud data extracted from GS-NIR reconstruction. The input point cloud is segmented by the segmentation module. Finally, the segmentation result is obtained.

Measurement of Phenotypic Data

Restoring the reconstructed 3D model of the neural radiation field to its actual scale and performing the final phenotypic measurements is another core task of this study. The NeRF model reconstruction is based on incremental position estimation. Previous studies on NeRF reconstruction often compressed the reconstructed data input with images to improve the training speed and model robustness. Although the model can maintain high

resolution and accuracy after reconstruction, it loses its actual scale and cannot acquire phenotypic data. To achieve this, scaling markers that are regular in shape and relatively complete must be found and identified. Firstly, an accurate calibration target is used as a marker to calibrate the reconstruction. Then, the point cloud of the calibration target is segmented using a point cloud segmentation network. Finally, the scale restoration factor between the length of the reconstructed calibration target and the actual length is measured as the scale of the corrected reconstruction. The estimation result is

$$\zeta = \frac{S_l}{S_{GS-NIR}}, \quad (10)$$

where ζ is the estimated scale restoration factor, S_l is the actual measured length and S_{GS-NIR} is the length of the reconstructed calibration from the GS-NIR.

3.4. Implementation Details

3.4.1. Hardware

In this study, two devices were employed to collect high-quality image data and high-precision point cloud data, as shown in Table 1. The first approach to image data acquisition utilises a GoPro Hero 11, an action camera with a high frame rate and high resolution by GoPro, Inc. (San Mateo, CA, USA), in order to facilitate the acquisition of data in a lightweight and speedy manner. This camera is capable of capturing 4K resolution images at a frame rate of 120 Hz, ensuring both quality and continuity in the data collection process. For each dataset, 100 images are extracted. Camera pose estimation and internal parameter computation are performed using Colmap [27]. The image data were mainly used for GS-NIR model reconstruction in this study.

Table 1. Technical parameters of the devices.

Devices	Parameter	Value
GoPro HERO11	Weight	149.00 g
	Resolution	4K+
	Lens stabilisation	Electronic
	Battery life	90 min
RVC-X mini	3D point cloud acquisition time	1.5
	Resolution	1.6 MP
	Recommended working distance (mm)	250–1500
	Camera weight (kg)	1.7
	Camera size (mm)	286 × 110 × 50
	Depth of field (mm)	100
	FOV (mm)	147 × 116
	XY-axis resolution (mm)	0.12
	Z-axis repeatability (mm)	0.03
	Z-axis measurement accuracy (mm)	0.003

Secondly, high-precision structured light is used to acquire point cloud data from the image. The robotic arm used is an xArm6, while the structured light 3D point cloud scanner is an RVC-X mini. The robotic arm equipped with the 3D scanner is programmed to follow a path around the target to be measured. At nine predetermined positions along this path, the arm stops, allowing the 3D scanner to perform a point cloud scan and document the current position of the arm. The point cloud data acquired by a high-precision 3D scanner are used in a standard size for this experiment to evaluate the reconstruction quality of the GS-NIR model.

3.4.2. Software

The automated phenotyping platform includes three components: (1) **Data acquisition:** The image acquisition module consists of a robotic arm equipped with a motion camera. The motion camera is capable of high-speed acquisition and maintains stability

to obtain high-quality images. (2) **Neural Implicit Surfaces Model**: The acquired images are subjected to camera position calculation and mask generation and finally input into the GS-NIR model. High-quality 3D reconstruction of coloured peppers is obtained from GS-NIR model. (3) **Phenotyping Processing Model**: Following reconstruction, phenotypic data are extracted from the plant model using a sparse segmentation network. The extraction network comprises 3D data preprocessing and a sparse semantic segmentation network. Finally, the scale restoration algorithm is incorporated to complete the phenotypic data measurement.

4. Results and Discussion

4.1. Experimental Setup

In this study, a robotic arm equipped with a high-precision 3D scanner was used to collect accurate position data for merging 3D point cloud data. Image data were simultaneously captured by a motion camera positioned at the same location. A standard agricultural dataset was used in the experiment. Initially, the robotic arm transported the sampling equipment and accurately controlled the sampling distance. The study recorded the exact position and corresponding 3D point cloud at each sampling location. The 3D point cloud data were then registered and fused, while the image data collected by the motion camera were reconstructed using the GS-NIR model to generate a high-fidelity reconstructed mesh. Finally, a 3D semantic segmentation network was integrated into this study to facilitate fruit phenotyping measurements.

4.1.1. Dataset Acquisition and Processing

This study's data were collected in November 2023 from the pepper planting greenhouses at Baiyun Experimental Base of Guangdong Academy of Agricultural Sciences as shown in Figure 6. The acquisition method uses a motion camera to acquire 2D image data and a 3D scanner to acquire 3D point cloud data. Each of the two sets of data were acquired for 30 scenes. Data were collected from peppers with varying growth processes and trait characteristics, including those with complex structures and occlusions, to evaluate the effectiveness of model reconstruction.



Figure 6. Illustrations of the standard scenarios for the agriculture and collection facilities.

4.1.2. Evaluation Method

The evaluation index continues to follow the previously used PSNR (Peak Signal-to-Noise Ratio) and adds more attention for the human eye to perceive the differences in the obvious SSIM (Structure Similarity Index Measure). The SSIM comes from brightness, contrast and structure, three indicators that comprehensively assess the quality of an image, to be able to make the closer to real for the human eye in order to assess the differences.

Brightness takes the mean value, image contrast takes the standard deviation and structural similarity takes the covariance, with the following formula:

$$SSIM(x, y) = \frac{(2\lambda_x\lambda_y + C_1)(2\sigma_{xy} + C_2)}{(\lambda_x^2 + \lambda_y^2 + C_1)(\sigma_x^2 + \sigma_y^2 + C_2)}. \quad (11)$$

In addition, the chamfer distance (CD), a commonly used evaluation metric in the field of 3D reconstruction, is introduced to assess the mesh reconstruction quality.

4.2. Ablation Studies

This section evaluates the effectiveness of the proposed three key designs in GS-NIR and shows their impact on the 3D reconstruction results. Firstly, the results of the complete model, including normals and meshes, are shown in Figure 7.



Figure 7. Reconstructions of the method on the Pepper dataset are demonstrated: (a) is the ground truth, (b) is the mesh with the colours removed and (c) is the mesh with normal direction, demonstrating high-quality mesh and accurate normals.

Geometric depth smoothing constraints: GS-NIR was trained without using any geometric depth constraints to understand the effect of constraints on the reconstruction quality. The results are shown in Figure 8a. Without geometric depth smoothing constraints, it was found that the presence of a large number of reflection points at certain locations on the pepper during model training led to the model incorrectly predicting the depth values during reconstruction, and the final reconstruction result obtained had a large number of holes. On real peppers, the whole is smooth and without holes, so a geometric depth smoothing constraint on the model is a reasonable solution.

Random dilation sampling: In GS-NIR, the sampled points become more important with the introduction of geometric depth smoothing constraints. Figure 8b shows the results without using random dilation sampling. Without using random dilation sampling, the fully random sampling strategy used throughout the model does not guarantee whether the sampled points are neighbouring or not, thus affecting the effectiveness of the geometric depth constraint. In addition, the strategy of sampling in pixel order was tested, which does not guarantee a large enough sampling area (an image with 640,000 pixels would result in a very long training time if calculated on the standard NeRF synthetic dataset of 80×800) and can only sample a very small area with guaranteed training efficiency, and the model will not converge in the end.

Adaptive scene module: In the experiments with the pepper scene, although the need for adaptive scene adjustment does not occur every time, this proposed adaptive scene module provides very good optimisation performance when the situation of poor camera viewpoints arises. Without the adaptive scene module, models will have a completely wrong depth estimation, and the whole model is difficult to converge. The results are shown in Figure 8c. Table 2 presents the results of the quantitative study.

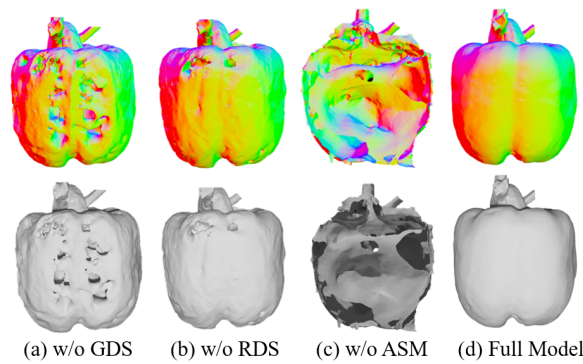


Figure 8. Qualitative studies of geometric depth smoothing constraints, random dilation sampling and adaptive scene module on the Pepper dataset. (a) is without geometric depth smoothing, (b) is without random dilation sampling and (c) is without adaptive scene module. Mesh is shown on top, normal mapping is shown on bottom.

Table 2. Quantitative studies of geometric depth smoothing constraints, random dilation sampling and adaptive scene module on the Pepper dataset.

	PSNR (dB)	SSIM	CD
w/o geometric depth smoothing	22.15	0.589	1.682
w/o random dilation sampling	25.68	0.693	1.347
w/o adaptive scene module	20.03	0.505	2.46
Full model (ours)	29.62	0.812	0.889

In addition, other fruit datasets were tested to demonstrate the versatility of GS-NIR in other scenarios. The results in Figure 9 show that GS-NIR obtains high-quality reconstruction for all types of fruits.

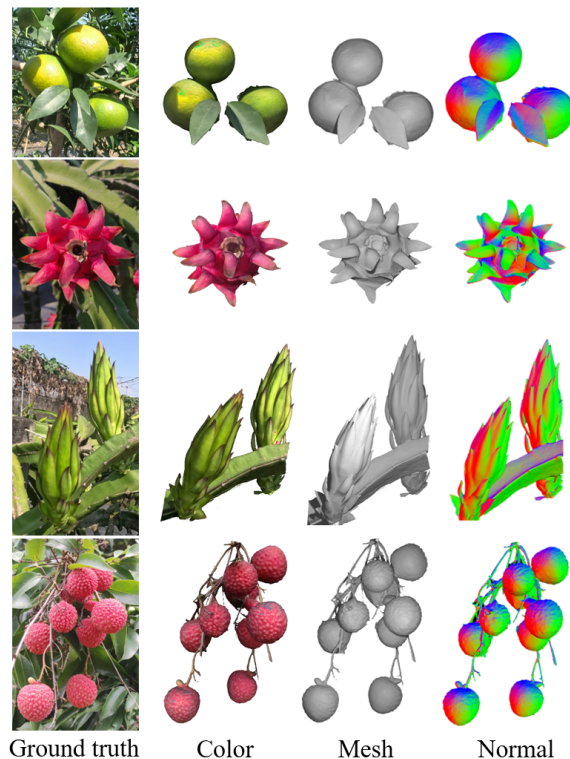


Figure 9. Illustration shows the high-quality reconstruction results of GS-NIR on orange, pitahaya, and litchi datasets, including colour mesh, mesh and normal.

4.3. Comparisons with Conventional NeRF-Based Approach

This experiment compares GS-NIR, Reality Capture, instant-NGP [35] and instant-NSR [38]. Reality Capture is one of the best software programs in terms of full-process integration and effectiveness of traditional MVS methods. Instant-NGP has the best rendering based on NeRF at present. It improves the rendering speed through an efficient coding method and concise MLP. Instant-NSR is the best reconstruction solution previously tested for obtaining high-quality meshes. Compared to instant-ngp, instant-NSR has a significant improvement in mesh quality because the SDF replaces the density in the reconstruction. Figure 10 shows the reconstruction details of the four methods.

In Table 3, the comparison of the three evaluation metrics in PSNR, SSIM, and CD is demonstrated. In the quantitative evaluation, this model outperforms the other methods with the pepper data. This shows that the proposed optimisation is effective.

From the experimental results, Instant-NGP, which uses neural networks for reconstruction, generally outperforms Reality Capture in terms of the reconstruction quality of coloured peppers, including PSNR, SSIM and reconstruction speed. The experimental results show that Instant-NGP is able to fit and merge the rendering very well with the neural network predictive density expression to obtain high-quality reconstruction models compared to Reality Capture. Instant-NSR is able to obtain better surface quality by using SDF. However, in the Pepper dataset, serious reconstruction flaws were encountered. GS-NIR can clearly be seen to improve reconstruction quality through various optimisations, and all the metrics in Table 3 are improved.

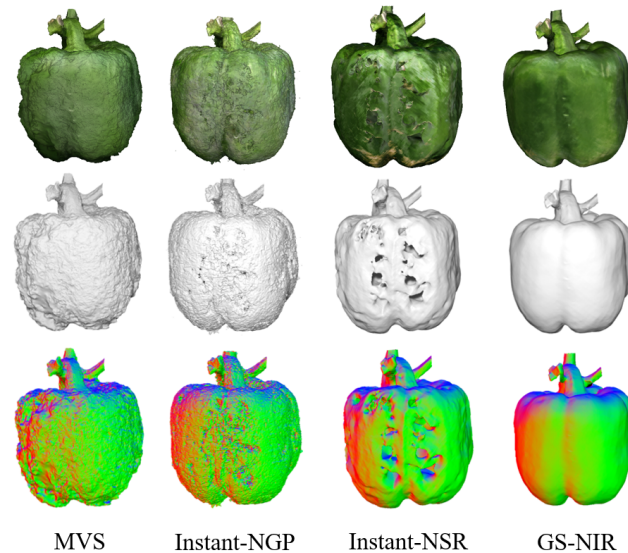


Figure 10. Illustration shows the qualitative analysis of the results of the four reconstruction methods: GS-NIR, Reality Capture, instant-NGP and instant-NSR.

Table 3. Average evaluation metrics of 3D reconstruction methods in the Pepper dataset.

Methods	PSNR	SSIM	CD	Train
Reality Capture (MVS)	26.52 dB	0.637	1.952	25 min
Instant-NGP	28.09 dB	0.725	2.421	2 min
Instant-NSR	26.89 dB	0.701	1.854	10 min
GS-NIR (ours)	29.74 dB	0.812	0.889	11 min

4.4. Quantitatively Evaluation on Reconstruction Accuracy

After the experimental comparisons above, the reconstruction quality of GS-NIR outperforms previous reconstruction methods based on image data. In this section, a point cloud of peppercorns was reconstructed using a high-precision 3D scanner, and this point cloud was compared with GS-NIR, Instant-NGP, and Instant-NSR as ground truth. The

average distance of the point cloud was used as a quantitative assessment metric, shown in Table 4, and Figure 11 demonstrates the effect of the qualitative analysis. Remarkably, compared to the state of the art, the method provides high-quality geometric surface reconstruction while maintaining a high-precision point cloud.

Table 4. Point distance comparison.

Methods	Mean Distance (mm)		
Instant-NGP	1.421	1.231	0.987
Instant-NSR	0.909	0.871	0.865
GS-NIR (ours)	0.799	0.827	0.805



Figure 11. (a–c) Illustration of matching results on three different samples by using the scanner method and GS-NIR model.

Meanwhile, in the process of acquiring point cloud data and reconstructing it using a 3D scanner, it was observed that scanning objects with smooth surfaces, such as peppers, can lead to several issues with the obtained point cloud data, as shown in Figure 12: (1) The object edges are often poorly reconstructed on the target edges because accurate reflections cannot be obtained from the smooth surface. (2) Differences in colour can be observed at different angles in ambient daytime lighting, which may result in uneven colours in the reconstructed point cloud. (3) The scanner produces many artefacts in low light. (4) Excessive light can cause strong reflective surfaces on smooth surfaces, which can seriously affect data acquisition and create voids in the reconstruction. All of these issues can affect the collection and measurement of plant phenotypes, resulting in inaccurate data. GS-NIR is based on multiview images and neural networks for reconstruction, which ensures the continuity and accuracy of the reconstructed scene and ultimately outputs a stable, high-fidelity mesh.

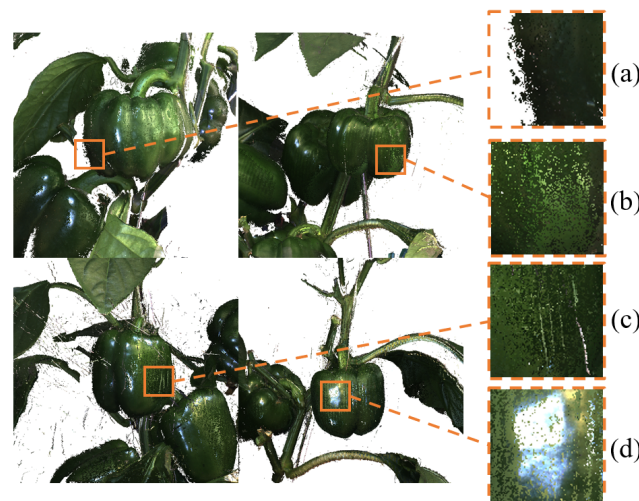


Figure 12. Illustration of the point cloud acquired by the 3D scanner and several problems with point cloud acquisition. (a) Bleeding points with cut edges on smooth surfaces. (b) Sampling chromatic aberration. (c) Insufficient light produces artefacts. (d) Reflections from highly reflective surfaces.

4.5. Demonstration on Phenotypic Measurements

This section demonstrates the measurement process of the proposed automated phenotyping platform, as illustrated in Figure 13. Previously, image data acquisition and 3D reconstruction was completed using the GS-NIR model to obtain a high-fidelity mesh. Subsequently, in order to obtain more accurate phenotypic data and to eliminate the interference of branches and leaves on the measurements, the 3D point cloud was segmented using Fuse-PointNet++ and extracted for the single pepper plant to be tested. In addition, one of the objectives was to obtain an accurate scale restoration factor. To this end, a calibration plate was added during data acquisition and reconstructed in 3D using the GS-NIR model. By accurately measuring the dimensions of the calibration plate, the scale restoration factor was calculated, and the actual scale of the pepper was restored.



Figure 13. Illustrations of phenotypic data collected from a point cloud after 3D semantic segmentation and scale restoration. (a) the GS-NIR model reconstructed 3D mesh with colours. (b) Results after 3D point cloud segmentation using Fuse-PointNet.

To assess the validity of the above experiments, phenotypic measurements were performed directly without scale reduction and point cloud segmentation. Without scale restoration, the model measurement error is almost 99%. Similarly, without point cloud segmentation, the accuracy of automated phenotype measurements decreases by 40%.

The data in Table 5 compare the three models and the 3D scanner with real measurements after scale restoration and point cloud segmentation. Point cloud data are measured accurately using CloudCompare. The experimental results show that this method outperforms Instant-NGP and Instant-NSR in terms of measurement accuracy, and it even outperforms 3D scanners. The error value of phenotype measurement is less than 1.5%.

Table 5. Comparison of phenotypic measurement data.

Methods	Height (mm)	Width (mm)	Difference
Actual measurement	73.0	74.9	
3D scanner	72.01	75.97	1.468%
Instant-NGP	69.55	70.86	5.149%
Instant-NSR	71.46	76.43	2.152%
GS-NIR (ours)	72.21	74.09	1.171%

4.6. Discussion

In this study, a new neural implicit surface model, GS-NIR, was proposed and an automated plant phenotyping platform was developed. GS-NIR is a simple and faster 3D reconstruction method, which obtains better reconstruction quality than conventional 3D scanners. This faster reconstruction method can overcome the difficulty of accessing heavy phenotype acquisition equipment in complex agricultural scenes. Phenotyping researchers no longer need expensive and inconvenient portable scanners. Instead, they can quickly collect phenotypic data in a short period of time by carrying only lightweight camera equipment.

4.6.1. Model Optimisation

A new neural implicit surface model, the geometric-smoothed neural implicit surface (GS-NIR), is proposed. The experimental results show that the performance of plant geometry reconstruction can be effectively improved by introducing smooth constraints and dilated sampling in the model. In contrast, the preimproved model is prone to reconstruction with holes or even failure. It was also verified that the new method is equally applicable to other fruit datasets.

4.6.2. Reconstruction Quality Assessment

A quantitative and qualitative comparison of the quality of GS-NIR and other NeRF-based reconstruction models revealed that GS-NIR is capable of obtaining a high-quality mesh of smooth-surface peppers. In the context of an actual phenotyping scenario, a comparison was conducted between the performance of GS-NIR and that of a 3D scanner. The results demonstrated that the reconstruction outcomes of GS-NIR were comparable to those of the 3D scanner.

4.6.3. Automated Phenotyping Measurements

Finally, an automated phenotype collection platform was developed. The platform integrates a data acquisition module and a 3D reconstruction module, and it introduces a scale restoration algorithm and a sparse neural network. The scale restoration algorithm enables the reconstruction results of the GS-NIR model to be restored to the actual scale, allowing us to extract accurate phenotypic data after reconstruction. The sparse neural network is used for semantic segmentation of the 3D point cloud, which improves the accuracy in acquiring phenotypic data in a natural orchard environment.

5. Conclusions

This study proposed a neural implicit surface reconstruction model, with a particular focus on the issues that arise in reconstruction due to the smooth surface of peppers. A comprehensive evaluation was conducted of GS-NIR and two SOTA NeRF-based methods. A comparison was also conducted with a 3D scanner in order to assess the accuracy of the

proposed method. The results demonstrate that the approach outperforms previous NeRF-based methods and achieves a comparable level of accuracy to that of the 3D scanner. Based on the above experiments, the scaling problem was successfully solved, the anti-interference ability was enhanced and an automated phenotype measurement platform was established. While this approach succeeds in accurate geometric reconstruction and normalisation of highly smooth fruits, the mapping of colours of the mesh will be challenging under extreme lighting conditions. Although this limitation has little impact on measuring the length and width of the plant body, it will be a constraint in subsequent phenotype extraction applications. Future work will focus on constructing GS-NIR models for real physical scenes to address the effects of lighting environments on mapping. In addition, there is potential to improve the training efficiency and quality of the models. Therefore, refining GS-NIR models and developing multimodal applications will be an important direction for future research.

Author Contributions: Conceptualisation, W.Y., K.H. and H.K.; methodology, W.Y.; software, W.Y.; investigation, W.Y.; formal analysis, W.Y.; data curation, A.A. and Z.Y.; validation, K.H. and A.A.; funding acquisition, J.Z.; resources, J.Z. and H.K.; supervision, J.Z. and H.K.; writing—review and editing, K.H., A.A. and Z.Y.; writing—original draft, W.Y. and J.Z. All authors have read and agreed to the published version of the manuscript.

Funding: The manuscript was supported by the National Natural Science Foundation of China (NSF) under grant number: 32372001.

Institutional Review Board Statement: Not applicable.

Data Availability Statement: The data presented in this study are available upon request from the authors.

Conflicts of Interest: The authors declare no conflicts of interest.

References

1. Sishodia, R.P.; Ray, R.L.; Singh, S.K. Applications of remote sensing in precision agriculture: A review. *Remote. Sens.* **2020**, *12*, 3136. [[CrossRef](#)]
2. Feng, L.; Chen, S.; Zhang, C.; Zhang, Y.; He, Y. A comprehensive review on recent applications of unmanned aerial vehicle remote sensing with various sensors for high-throughput plant phenotyping. *Comput. Electron. Agric.* **2021**, *182*, 106033. [[CrossRef](#)]
3. Fu, L.; Gao, F.; Wu, J.; Li, R.; Karkee, M.; Zhang, Q. Application of consumer RGB-D cameras for fruit detection and localization in field: A critical review. *Comput. Electron. Agric.* **2020**, *177*, 105687. [[CrossRef](#)]
4. Schauer, N.; Fernie, A.R. Plant metabolomics: Towards biological function and mechanism. *Trends Plant Sci.* **2006**, *11*, 508–516. [[CrossRef](#)] [[PubMed](#)]
5. Schulze, W.X.; Usadel, B. Quantitation in mass-spectrometry-based proteomics. *Annu. Rev. Plant Biol.* **2010**, *61*, 491–516. [[CrossRef](#)] [[PubMed](#)]
6. Meraj, T.; Sharif, M.I.; Raza, M.; Alabrah, A.; Kadry, S.; Gandomi, A.H. Computer vision-based plants phenotyping: A comprehensive survey. *Iscience* **2024**, *27*, 108709. [[CrossRef](#)] [[PubMed](#)]
7. Zhang, Y.; Zhang, N. Imaging technologies for plant high-throughput phenotyping: A review. *Front. Agric. Sci. Eng.* **2018**, *5*, 406–419. [[CrossRef](#)]
8. Lou, L.; Liu, Y.; Shen, M.; Han, J.; Corke, F.; Doonan, J.H. Estimation of branch angle from 3D point cloud of plants. In Proceedings of the 2015 International Conference on 3D Vision, Lyon, France, 19–22 October 2015; pp. 554–561.
9. Kolhar, S.; Jagtap, J. Plant trait estimation and classification studies in plant phenotyping using machine vision-A review. *Inf. Process. Agric.* **2023**, *10*, 114–135. [[CrossRef](#)]
10. Paturkar, A.; Gupta, G.S.; Bailey, D. 3D reconstruction of plants under outdoor conditions using image-based computer vision. In *Recent Trends in Image Processing and Pattern Recognition: Proceedings of the Second International Conference, RTIP2R 2018, Solapur, India, 21–22 December 2018, Revised Selected Papers, Part III* 2; Springer: Berlin/Heidelberg, Germany, 2019; pp. 284–297.
11. Harandi, N.; Vandenberghe, B.; Vankerschaver, J.; Depuydt, S.; Van Messem, A. How to make sense of 3D representations for plant phenotyping: A compendium of processing and analysis techniques. *Plant Methods* **2023**, *19*, 60. [[CrossRef](#)] [[PubMed](#)]
12. Mildenhall, B.; Srinivasan, P.P.; Tancik, M.; Barron, J.T.; Ramamoorthi, R.; Ng, R. Nerf: Representing scenes as neural radiance fields for view synthesis. *Commun. ACM* **2021**, *65*, 99–106. [[CrossRef](#)]
13. Hu, K.; Ying, W.; Pan, Y.; Kang, H.; Chen, C. High-fidelity 3D reconstruction of plants using Neural Radiance Fields. *Comput. Electron. Agric.* **2024**, *220*, 108848. [[CrossRef](#)]

14. Zhang, M.; Xu, S.; Han, Y.; Li, D.; Yang, S.; Huang, Y. High-throughput horticultural phenomics: The history, recent advances and new prospects. *Comput. Electron. Agric.* **2023**, *213*, 108265. [[CrossRef](#)]
15. Li, Y.; Fan, X.; Mitra, N.J.; Chamovitz, D.; Cohen-Or, D.; Chen, B. Analyzing growing plants from 4D point cloud data. *ACM Trans. Graph.* **2013**, *32*, 1–10. [[CrossRef](#)]
16. Kazmi, W.; Foix, S.; Alenyà, G.; Andersen, H.J. Indoor and outdoor depth imaging of leaves with time-of-flight and stereo vision sensors: Analysis and comparison. *ISPRS J. Photogramm. Remote. Sens.* **2014**, *88*, 128–146. [[CrossRef](#)]
17. Paulus, S.; Dupuis, J.; Riedel, S.; Kuhlmann, H. Automated analysis of barley organs using 3D laser scanning: An approach for high throughput phenotyping. *Sensors* **2014**, *14*, 12670–12686. [[CrossRef](#)] [[PubMed](#)]
18. Su, Q.; Kondo, N.; Li, M.; Sun, H.; Al Riza, D.F. Potato feature prediction based on machine vision and 3D model rebuilding. *Comput. Electron. Agric.* **2017**, *137*, 41–51. [[CrossRef](#)]
19. Chaivivatrakul, S.; Tang, L.; Dailey, M.N.; Nakarmi, A.D. Automatic morphological trait characterization for corn plants via 3D holographic reconstruction. *Comput. Electron. Agric.* **2014**, *109*, 109–123. [[CrossRef](#)]
20. Kang, H.; Chen, C. Fast implementation of real-time fruit detection in apple orchards using deep learning. *Comput. Electron. Agric.* **2020**, *168*, 105108. [[CrossRef](#)]
21. Kang, H.; Zang, Y.; Wang, X.; Chen, Y. Uncertainty-driven spiral trajectory for robotic peg-in-hole assembly. *IEEE Robot. Autom. Lett.* **2022**, *7*, 6661–6668. [[CrossRef](#)]
22. Paulus, S.; Dupuis, J.; Mahlein, A.K.; Kuhlmann, H. Surface feature based classification of plant organs from 3D laserscanned point clouds for plant phenotyping. *BMC Bioinform.* **2013**, *14*, 238. [[CrossRef](#)]
23. Kang, H.; Wang, X.; Chen, C. Accurate Fruit Localisation for robotic harvesting using high resolution LiDAR-camera fusion. *arXiv* **2022**, arXiv:2205.00404.
24. Kang, H.; Wang, X. Semantic segmentation of fruits on multi-sensor fused data in natural orchards. *Comput. Electron. Agric.* **2023**, *204*, 107569. [[CrossRef](#)]
25. Kjaer, K.H.; Ottosen, C.O. 3D laser triangulation for plant phenotyping in challenging environments. *Sensors* **2015**, *15*, 13533–13547. [[CrossRef](#)] [[PubMed](#)]
26. Li, Z.; Guo, R.; Li, M.; Chen, Y.; Li, G. A review of computer vision technologies for plant phenotyping. *Comput. Electron. Agric.* **2020**, *176*, 105672. [[CrossRef](#)]
27. Schonberger, J.L.; Frahm, J.M. Structure-from-motion revisited. In Proceedings of the IEEE Conference on Computer Vision and Pattern Recognition, Las Vegas, NV, USA, 27–30 June 2016; pp. 4104–4113.
28. Xiong, J.; He, Z.; Lin, R.; Liu, Z.; Bu, R.; Yang, Z.; Peng, H.; Zou, X. Visual positioning technology of picking robots for dynamic litchi clusters with disturbance. *Comput. Electron. Agric.* **2018**, *151*, 226–237. [[CrossRef](#)]
29. Jay, S.; Rabatel, G.; Hadoux, X.; Moura, D.; Gorretta, N. In-field crop row phenotyping from 3D modeling performed using Structure from Motion. *Comput. Electron. Agric.* **2015**, *110*, 70–77. [[CrossRef](#)]
30. Zermas, D.; Morellas, V.; Mulla, D.; Papanikopoulos, N. 3D model processing for high throughput phenotype extraction—The case of corn. *Comput. Electron. Agric.* **2020**, *172*, 105047. [[CrossRef](#)]
31. Gao, Y.; Wang, Q.; Rao, X.; Xie, L.; Ying, Y. OrangeStereo: A navel orange stereo matching network for 3D surface reconstruction. *Comput. Electron. Agric.* **2024**, *217*, 108626. [[CrossRef](#)]
32. Ma, H.; Zhu, X.; Ji, J.; Wang, H.; Jin, X.; Zhao, K. Rapid estimation of apple phenotypic parameters based on 3D reconstruction. *Int. J. Agric. Biol. Eng.* **2021**, *14*, 180–188. [[CrossRef](#)]
33. Yang, H.; Hu, Y.; Lan, Y.; Zhang, P.; He, Y.; Zhou, Z.; Chen, J. A new alternative for assessing ridging information of potato plants based on an improved benchmark structure from motion. *Comput. Electron. Agric.* **2023**, *213*, 108220. [[CrossRef](#)]
34. Kerbl, B.; Kopanas, G.; Leimkühler, T.; Drettakis, G. 3D Gaussian Splatting for Real-Time Radiance Field Rendering. *ACM Trans. Graph.* **2023**, *42*, 139-1–139-14. [[CrossRef](#)]
35. Müller, T.; Evans, A.; Schied, C.; Keller, A. Instant neural graphics primitives with a multiresolution hash encoding. *ACM Trans. Graph.* **2022**, *41*, 1–15. [[CrossRef](#)]
36. Wang, P.; Liu, L.; Liu, Y.; Theobalt, C.; Komura, T.; Wang, W. Neus: Learning neural implicit surfaces by volume rendering for multi-view reconstruction. *arXiv* **2021**, arXiv:2106.10689.
37. Yariv, L.; Gu, J.; Kasten, Y.; Lipman, Y. Volume rendering of neural implicit surfaces. *Adv. Neural Inf. Process. Syst.* **2021**, *34*, 4805–4815.
38. Zhao, F.; Jiang, Y.; Yao, K.; Zhang, J.; Wang, L.; Dai, H.; Zhong, Y.; Zhang, Y.; Wu, M.; Xu, L.; et al. Human performance modeling and rendering via neural animated mesh. *ACM Trans. Graph.* **2022**, *41*, 1–17. [[CrossRef](#)]
39. Wang, Y.; Han, Q.; Habermann, M.; Daniilidis, K.; Theobalt, C.; Liu, L. Neus2: Fast learning of neural implicit surfaces for multi-view reconstruction. In Proceedings of the IEEE/CVF International Conference on Computer Vision, Paris, France, 2–3 October 2023; pp. 3295–3306.
40. Li, Z.; Müller, T.; Evans, A.; Taylor, R.H.; Unberath, M.; Liu, M.Y.; Lin, C.H. Neuralangelo: High-fidelity neural surface reconstruction. In Proceedings of the IEEE/CVF Conference on Computer Vision and Pattern Recognition, Vancouver, BC, Canada, 17–24 June 2023; pp. 8456–8465.

41. Kang, H.; Chen, C. Fruit detection, segmentation and 3D visualisation of environments in apple orchards. *Comput. Electron. Agric.* **2020**, *171*, 105302. [[CrossRef](#)]
42. Qi, C.R.; Yi, L.; Su, H.; Guibas, L.J. Pointnet++: Deep hierarchical feature learning on point sets in a metric space. In Proceedings of the 31st Annual Conference on Neural Information Processing Systems (NIPS 2017), Long Beach, CA, USA, 4–9 December 2017.

Disclaimer/Publisher’s Note: The statements, opinions and data contained in all publications are solely those of the individual author(s) and contributor(s) and not of MDPI and/or the editor(s). MDPI and/or the editor(s) disclaim responsibility for any injury to people or property resulting from any ideas, methods, instructions or products referred to in the content.